Online Monitoring of the Osiris Reactor with the Nucifer Neutrino Detector

G. Boireau,[1] L. Bouvet,[1] A.P. Collin,[1] G. Coulloux,[1] M. Cribier,[1] H. Deschamp,[1] V. Durand,[1] M. Fechner,[1] V. Fischer,[1] J. Gaffiot,[1] N. Gérard Castaing,[1] R. Granelli,[1] Y. Kato,[1] T. Lasserre,[1] L. Latron,[1] P. Legou,[1] A. Letourneau,[1] D. Lhuillier,[1] G. Mention,[1] Th. A. Mueller,[1] T-A. Nghiem,[1] N. Pedrol,[1] J. Pelzer,[1] M. Pequignot,[1] Y. Piret,[1] G. Prono,[1] L. Scola,[1] P. Starzinski,[1] M. Vivier,[1] E. Dumonteil,[2] D. Mancusi,[2] C. Varignon,[3] C. Buck,[4] M. Lindner,[4] J. Bazoma,[5] S. Bouvier,[5] V.M. Bui,[5] V. Communeau,[5] A. Cucoanes,[5] M. Fallot,[5] M. Gautier,[5] L. Giot,[5] G. Guilloux,[5] M. Lenoir,[5] J. Martino,[5] G. Mercier,[5] T. Milleto,[5] N. Peuvrel,[5] A. Porta,[5] N. Le Quéré,[5] C. Renard,[5] L.M. Rigalleau,[5] D. Roy,[5] T. Vilajosana,[5] and F. Yermia[5]

(The Nucifer Collaboration)

[1] *Commissariat à l'énergie atomique et aux énergies alternatives, Centre de Saclay, DSM/IRFU, 91191 Gif-sur-Yvette, France*
[2] *Commissariat à l'énergie atomique et aux énergies alternatives, Centre de Saclay, DEN, 91191 Gif-sur-Yvette, France*
[3] *Commissariat à l'énergie atomique et aux énergies alternatives, DAM, DIF, 91297, Arpajon, France*
[4] *Max-Planck-Institut für Kernphysik, 69029 Heidelberg, Germany*
[5] *SUBATECH, CNRS/IN2P3, Université de Nantes, Ecole des Mines de Nantes, F-44307 Nantes, France*

Originally designed as a new nuclear reactor monitoring device, the Nucifer detector has successfully detected its first neutrinos. We provide the second shortest baseline measurement of the reactor neutrino flux. The detection of electron antineutrinos emitted in the decay chains of the fission products, combined with reactor core simulations, provides a new tool to assess both the thermal power and the fissile content of the whole nuclear core and could be used by the International Agency for Atomic Energy (IAEA) to enhance the Safeguards of civil nuclear reactors. Deployed at only 7.2 m away from the compact Osiris research reactor core (70 MW) operating at the Saclay research centre of the French Alternative Energies and Atomic Energy Commission (CEA), the experiment also exhibits a well-suited configuration to search for a new short baseline oscillation. We report the first results of the Nucifer experiment, describing the performances of the $\sim 0.85\,\mathrm{m}^3$ detector remotely operating at a shallow depth equivalent to ~ 12 m of water and under intense background radiation conditions. Based on 145 (106) days of data with reactor ON (OFF), leading to the detection of an estimated 40 760 $\overline{\nu}_\mathrm{e}$, the mean number of detected antineutrinos is $281 \pm 7(\mathrm{stat}) \pm 18(\mathrm{syst})\,\overline{\nu}_\mathrm{e}$/day, in agreement with the prediction $277 \pm 23\,\overline{\nu}_\mathrm{e}$/day. Due to the large background no conclusive results on the existence of light sterile neutrinos could be derived, however. As a first societal application we quantify how antineutrinos could be used for the Plutonium Management and Disposition Agreement.

I. INTRODUCTION

In a context of increasing needs for carbon emission-free energy, civilian nuclear power generation has the potential to play an important role in global energy production, and the list of countries aiming to acquire technological know-how in the field of civilian nuclear energy could increase. As a consequence, the International Atomic Energy Agency (IAEA) has been evaluating the potential of new technologies to guarantee that nations use nuclear energy only for peaceful purposes.

Neutrino detectors have the unique ability to non-intrusively monitor a nuclear reactor's operational status, thermal power and fissile content in real-time, from outside the reactor containment. More specifically the scenarios of interest are to confirm the absence of unrecorded production of fissile materials in declared reactors as well as to estimate the total burn-up[1] of a reactor core. Nucifer is a detector first built for long term reliable safeguards measurements in the vicinity of operating nuclear reactor cores. The experiment aims at demonstrating the concept of "neutrinometry" at the pre-industrialized stage. Therefore a well-established technology and commercial components were chosen for the detection system.

In addition, after the re-evaluation of antineutrino spectra [2–4], the reanalysis of all short baseline reactor experiments [5] lead to what is known as the Reactor Antineutrino Anomaly (RAA) with $R_\nu^{\mathrm{obs}}/R_\nu^{\mathrm{pred}} = 0.936 \pm 0.024$ [6]. And it turns out that the Nucifer experimental set-up is adequate to probe the Reactor Antineutrino Anomaly [5], searching for possible oscillations into sterile neutrino species at very short baselines. Indeed, Nucifer is a compact detector (~ 1.2 m in diameter, 0.7 m in height), deployed at only 7.21 ± 0.11 m (centre to centre) from a compact nuclear core ($57 \times 57 \times 60\,\mathrm{cm}^3$). Therefore the three conditions to search for short baseline oscillations are met. Nucifer is even the second shortest baseline reactor neutrino experiment, the only closest experiment being a 3.2 L Gd-loaded liquid scintillator detector deployed at only 6.5 m from the Savannah River Plant (USA) in 1965 [7, 8]. The third shortest baseline is the ILL experiment [9] with 377 L of liquid scintillator at 8.76 m from the core, which lead to a ratio of experimental to expected integral positron yield of $0.832 \pm 3.5\,\%(\mathrm{stat}) \pm 8.87\,\%(\mathrm{syst})$ as stated in the 1995 reanalysis [10].

Among the possible societal applications the Plutonium Management and Disposition Agreement (PMDA) [11] could be monitored through neutrino

rate monitoring. Indeed, in this procedure, weapon-grade plutonium could be processed into Mixed OXide uranium-plutonium (MOX) fuel, irradiated in civil nuclear power reactors, and therefore transformed into material unusable in the fabrication of nuclear weapons.

The paper first describes the experimental lay-out in part II, from the Osiris reactor to the data acquisition system through the Nucifer detector. We then calculate the expected signal and its associated errors in part III, accounting for the major part of the final uncertainty due to the relatively low detector efficiency. Then the calibration system is depicted in part IV, followed by the data analysis: we detail the data sample in section V A and the neutrino candidate selection in section V B, then the accidental background in section V C, the cosmic induced correlated background in section V D, the reactor induced correlated backgrounds in section V E and finally the detection efficiency and the associated uncertainties in section V F. We thus present the Nucifer results at Osiris in part VI, summarized by the ratio of observed to expected neutrino detection rate. We finally discuss a potential application for the PMDA agreement, using Nucifer's collected data, in part VII.

II. EXPERIMENTAL LAYOUT

A. Deployment site: the Osiris reactor

Nucifer is installed on the concrete foundation slab of the Osiris reactor building, 11 meters beneath the water pool level, in a dedicated room next to the reactor core (see Fig. 1). Such a location allows to safely support the weight of the detector together with its heavy passive shielding ($\gtrsim 62$ tonnes). It also offers a modest overburden, reducing the muon flux by a factor of 2.7 with respect to sea level. The overburden is equivalent to ~ 12 meters of water.

The reactor core, approximately at the Nucifer room ceiling level, is located 7.21 ± 0.11 m away from the detector, from the centre of the core to the centre of the detector. In this configuration radiations from the reactor core are attenuated by about 2 m of concrete and 3.5 m of water. Nevertheless, the level of gamma radiations in the Nucifer room is still quite high during the reactor operations, enhancing the challenge of properly extracting the neutrino flux.

Osiris is a light water experimental reactor of open-core pool type located at the Saclay research centre of the French Alternative Energies and Atomic Energy Commission (CEA). It operates at a nominal thermal power of 70 MW and has been designed for technological irradiation purposes and radioisotope production [12]. The fissile elements produce a high neutron flux in the core, at the level of a few 10^{14} neutrons cm^{-2} s^{-1}, both in the thermal and fast energy range. The core size is $57 \times 57 \times 60$ cm^3, excluding its vessel, corresponding to 56 cells loaded with 38 standard fuel elements (U_3Si_2Al plates enriched at 19.75 % in ^{235}U), 6 control elements (made of Hafnium absorber in the upper part and of fuel in the lower part), 7 Beryllium elements used as neutron reflectors, and 5 cells equipped with water boxes dedicated to experiments. The cells are arranged in a square lattice with a lattice parameter of 8.74 cm. The absence of pressurization vessel allows for a direct access to the core at any time.

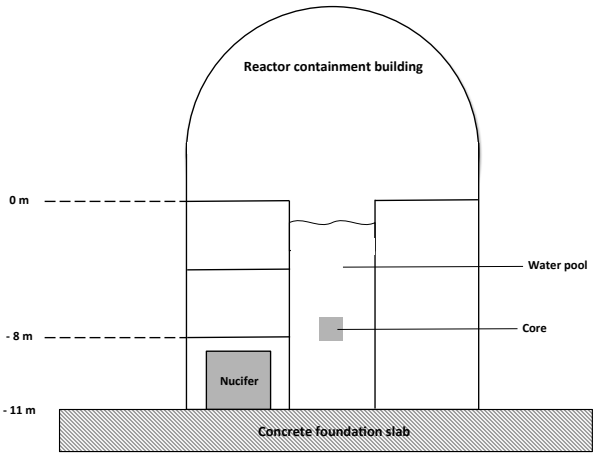

FIG. 1. The Nucifer experimental layout. The detector centre is located 7.21 ± 0.11 m away from the reactor core centre. East is on the right, south points to the reader.

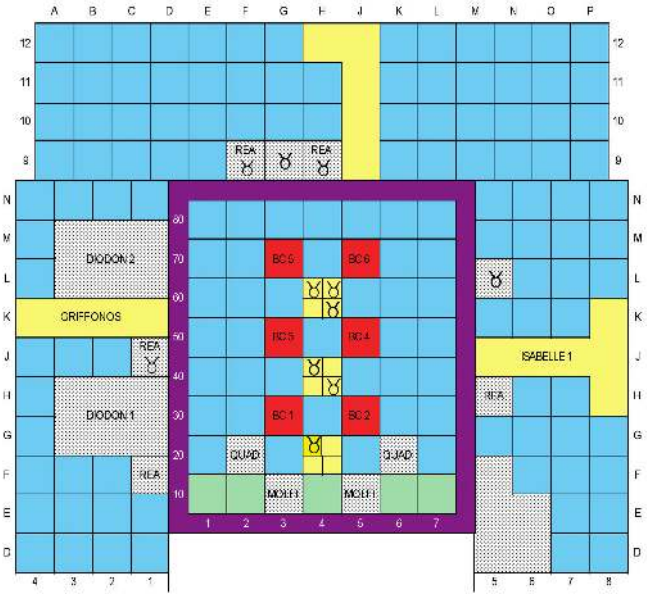

FIG. 2. Top scheme of the Osiris core. "BC" squares (red) stand for core control elements, bottom core line squares (labelled 10, green) for Beryllium reflector elements. The square surrounding the core (purple) represents the steel vessel. Other areas (yellow, grey) stand for locations used for experimental irradiation devices, or industrial irradiation locations [13]. North is on top, Nucifer is located on the left.

Osiris typically operates 180 days per year with 3 week reactor cycles, core being refuelled by about $1/7^{th}$. The 19.75 % enrichment of the nuclear fuel in ^{235}U and the short cycle duration suppress the evolution of the isotopic composition of the nuclear fuel. To start the reactor, control rods 1, 2, 5 and 6 are first raised, and the core reaches criticality during the raising of the next rod which can be the 3 or the 4 (see fig 2). This rod is then raised to the top within the next few days, and the last rod is progressively raised during the remaining part of the cycle. This sequence leads to a displacement of the fission barycentre, in the east/west direction and vertically, different for the two rod configurations (3 then 4 or 4 then 3).

B. Nucifer detector

The Nucifer detector (Fig. 3) consists of a cylindrical liquid scintillator tank, surrounded by an active plastic scintillator veto to tag cosmic ray muons, and two layers of shielding: 14 cm of boron-doped polyethylene to capture neutrons, and 10 cm of lead layer to attenuate external gamma rays.

Three additional lead walls have been erected to further attenuate the reactor induced gamma rays. A first 10 cm thick wall was originally installed between the detector and the reactor wall, on the east direction side (see Fig. 1). Then a second 4 cm thick wall was later built between the original lead wall and the reactor wall to further reduce the amount of gamma rays originating directly from the core (see section V C) resulting in a factor of 3 additional attenuation.

Finally, a third 10 cm thick wall was erected on the southern side of the detector (see Fig. 1) to suppress the gamma radiations coming from the primary water loop of the reactor cooling circuit located behind the 1 m thick concrete wall of the detector casemate. Indeed when flowing through the fuel elements, the water of this circuit is being highly activated by the fast neutron flux inside the core. ^{16}N is produced through (n, p) reaction on ^{16}O of the water [14] and subsequently decay with a 7.13 s half-life emitting a 6.1 MeV γ-ray with an intensity of 67 % (plus a 7.1 MeV γ-ray with intensity 4.9 %). A dedicated circuit, located partly behind the southern wall of the Nucifer casemate, delays its arrival to the primary pumps by about 90 s, giving time for ^{16}N to decay completely. The effect of this added shielding was to reduce the single event rate by more than an order of magnitude.

The liquid scintillator is contained inside a stainless steel cylindrical vessel (1404.2 mm in height, 1250.4 mm in diameter). The internal surface of this vessel is coated with reflective white Teflon, chosen for its chemical compatibility with the liquid scintillator as well as for increasing visible light collection. The tank contains 846.8 ± 7.0 L of liquid scintillator doped with a Gadolinium complex (a Gd-beta-diketonate) to enhance the capture of thermal neutrons and sign the neutron capture.

The chemistry of the Nucifer scintillator is based on the target liquid of the Double Chooz experiment [15], with three main modifications. First the Gd-concentration was increased to 0.17 % in mass to reduce the capture time of thermal neutrons (τ_n), expected to be in the range of 20 µs. Second the concentration of o-PXE (ortho-Phenylxylylethane) in the scintillator was increased to 57 % in volume, the remaining 43 % being dodecane. In this way light yield and pulse shape discrimination power for rejection of correlated background events are improved. Finally, the concentration of the primary fluor PPO (2,5-Diphenyloxazole) was slightly increased to compensate for light losses due to the higher Gd concentration [15]. However, the concentration of the secondary fluor bis-MSB (1,4-Bis(2-MethylStyryl)Benzene) was kept at 20 mg/l.

The light collection is performed by sixteen 8-inch photomultipliers (PMTs), type Hammamatsu R5912, located at the top of the detector vessel. A 25 cm thick acrylic disk separates the PMTs from the target liquid scintillator. Filled with mineral oil, this so-called buffer optically couples the PMTs to the liquid scintillator. This design allows a good uniformity of the detector response to energy deposition in the whole target volume and shields the scintillator from the intrinsic PMT radioactivity. The buffer is fixed to the tank lid. No phenomenon of light emission from PMTs was detected (so-called "flashing PMTs").

A light injection system guiding light from LED to Teflon diffusers in the tank through optical fibres allows the monitoring of the PMT gain as well as the liquid optical properties, thanks to several types of light diffusers. In addition small encapsulated radioactive sources can be deployed along the target central axis inside a vertical stainless steel tube externally coated with Teflon.

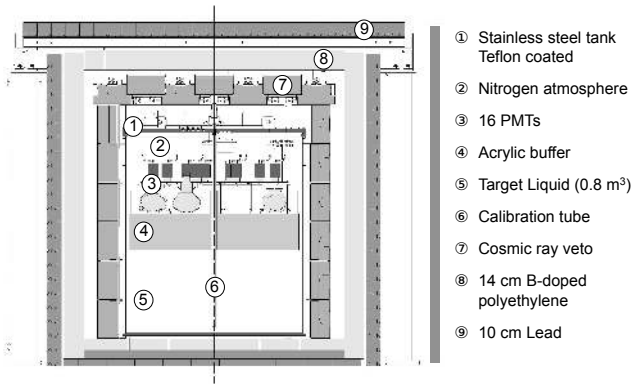

FIG. 3. Cut view of the Nucifer detector. The overall volume is about $3 \times 3 \times 2.4\,\mathrm{m}^3$.

The muon veto is made of 32 modular detectors, each one containing a 5 cm thick plastic scintillator bar (150 to 170 cm length, 25 cm width) associated to a single PMT decoupled from its surface. The plastic scintillator thickness and light collection were optimized in order to discriminate cosmic muons from high energy gamma

rays in a compact and cost-effective way. Indeed, muon energy deposition is at least 10 MeV, corresponding to perpendicularly crossing muons at the minimum ionizing point, while the highest gamma energy is also 10 MeV, from neutron capture on metals surrounding the detector or in the concrete. Using events that saturate all PMTs in the Nucifer vessel and checking if the muon veto had triggered or not, we measured a muon detection efficiency of 97 %.

C. Electronics and data acquisition

The analogical output of each of the 16 PMTs is split in 4 different channels. The first channel is used to build the trigger (the analogical sum of all PMTs), and the second channel is routed to a constant fraction discriminator to get the time information. The two last channels are delayed and sent to commercial CAEN Charge to Digital Converter (QDC) modules. One integration gate is adjusted to integrate the full signal centred around a 150 ns time window. The other gate is delayed by about 40 ns to integrate only the late component of the signal. The comparison of the resulting two charges can be later used for Pulse Shape Discrimination (PSD).

The acquisition is triggered either by the analogical sum of all PMTs overcoming a threshold equivalent to about 1 MeV, or by any of the muon veto module overcoming a threshold equivalent to about 10 MeV, or by computer driven LED and random signals. The dead time is computed online by counting internal clock pulses inhibited by all hardware vetos (such as QDC busy gates or saturation of the buffers of the QDC/TDC).

The Data Acquisition system (DAQ) is based on the LabVIEW software allowing a remote control of the acquisition and a constant monitoring of the safety parameters, such as pressure, liquid level and temperature at various locations. The data stream is automatically chopped up in 500 MB runs and transferred to the CC-IN2P3 computing centre for storage and off-line analysis. Typical run duration is 43 minutes with the Osiris reactor operating at full power, and 53 minutes when the reactor is not operating. The difference comes from the reactor induced gamma background in the Nucifer tank.

In case of a significant deviation of any set of predefined parameters, warning emails are automatically sent to on-call experts. If the deviation exceeds a higher threshold, an alarm is sent to the reactor control room. Since its installation at Osiris in Spring 2012, the Nucifer detector has been operating without any safety failure.

III. EXPECTED SIGNAL

A. Theoretical neutrino rate

The detection of Osiris antineutrinos is achieved through the Inverse Beta Decay (IBD) reaction on the liquid scintillator free protons: $\bar{\nu_e} + p \rightarrow e^+ + n$, taking advantage of the time delayed coincidence between the positron and neutron signals. The positron detection is the prompt signal, its energy is related to the neutrino's by: $\mathrm{E_{prompt}} \sim \mathrm{E}_{\bar{\nu_e}} - 0.782\,\mathrm{MeV}$. Then the neutron is captured with high efficiency either on Gd or H atoms in the liquid scintillator. Neutron captures occur with a mean time of about 20 µs and lead to the emission of a few γ-rays with a total energy of 8.05 MeV in average for Gd natural isotopic composition and thermal neutron capture at ambient temperature.

To first order, the number of neutrino events detected per day depends on the neutrino flux emitted by the reactor, the baseline, the number of target free protons, and the detector efficiency. The neutrino flux depends on the reactor thermal power and, since different fissioning isotopes lead to different neutrino spectra, on the fission fractions (see Fig. 15). Finally, the event rate at a given time t is given by

$$\tau_{\bar{\nu}}(t) = \frac{P_{\mathrm{th}}(t)}{\sum_k \alpha_k(t) E_k}\, \rho_p \sum_k \alpha_k(t) \int_0^\infty \sigma_{\bar{\nu_e}}(E) S_k(E)\, l_{\mathrm{eff}}\, \mathrm{d}E \tag{1}$$

The first term describes the number of fissions per unit time with $P_{\mathrm{th}}(t)$ the thermal power, $\alpha_k(t)$ the fission fraction of isotope k ($k = {}^{235}\mathrm{U},\ {}^{238}\mathrm{U},\ {}^{239}\mathrm{Pu},\ {}^{241}\mathrm{Pu}$) and E_k the mean energy per fission of isotope k. ρ_p is the proton density in the liquid scintillator. The integral on the antineutrino energy represents the mean fission cross-section with $\sigma_{\bar{\nu_e}}(E)$ the IBD cross section and $S_k(E)$ the fission spectrum of isotope k in units of $\overline{\nu}_{\mathrm{e}}\,\mathrm{fission}^{-1}\,\mathrm{MeV}^{-1}$ [16].

The effective length l_{eff} is homogeneous to a distance and takes into account the finite extensions of both the core and the detector, a necessary refinement due to the very short baseline of the experiment. It is defined as

$$l_{\mathrm{eff}} = \iiint_{\mathscr{V}_{\mathrm{c}}} \Psi_{\mathrm{f},k}(t, \overrightarrow{r_{\mathrm{c}}}) \iiint_{\mathscr{V}_{\mathrm{d}}} \frac{\varepsilon(E, \overrightarrow{r_{\mathrm{d}}})}{4\pi\,(\overrightarrow{r_{\mathrm{d}}} - \overrightarrow{r_{\mathrm{c}}})^2}\, \mathrm{d}^3\overrightarrow{r_{\mathrm{d}}}\, \mathrm{d}^3\overrightarrow{r_{\mathrm{c}}} \tag{2}$$

with $\Psi_{\mathrm{f},k}(t, \overrightarrow{r_{\mathrm{c}}})$ the fission density of isotope k, normalized to one fission, $\mathscr{V}_{\mathrm{c}}$ the reactor core volume, $\mathscr{V}_{\mathrm{d}}$ the detector volume, $\varepsilon(E, \overrightarrow{r_{\mathrm{d}}})$ the detection efficiency, $\overrightarrow{r_{\mathrm{c}}}$ a vector pointing to a given point in the core and $\overrightarrow{r_{\mathrm{d}}}$ a vector pointing to a given point in the detector. In the case of point-like core and detector one readily recovers the equivalence $\rho_p l_{\mathrm{eff}} \equiv \mathcal{N}_p / 4\pi L^2$ with $\mathcal{N}_p$ the number of protons in the target and L the mean baseline.

B. Parameters and associated uncertainties

All relevant reactor operating parameters are being provided by the Osiris facility, with a 5 min period, leading to an average thermal power of 66.5 MW. From the enthalpy balance performed online on the primary circuit of reactor we estimate a 2 % relative uncertainty [17].

Furthermore the layout and burn-up of each assembly is made available, at the beginning of each reactor cycle. Detailed core simulations are then performed with the 3D Monte-Carlo code TRIPOLI-4® [18]. We studied two core configurations, corresponding to the two typical initial burn-up maps of Osiris with either the control rod number 3 or 4 used as the last rod to control the reactor power. For each configuration two extreme positions of the control rods, at the beginning and end of the cycle, have been considered. During the cycle, the translation of the barycentre of the fissions due to the control rods is only 2.5 cm, so the deviation from the average barycentre of the fissions is negligible. The corresponding impact on the interaction rate is inferior to 0.3 %.

Between the two initial control rod sequences, the mean barycentre of the fissions is shifted by 3.6 cm at the beginning of a cycle and 1.1 cm at the end, leading to a difference in the predicted rate inferior to 1 %. Still this effect is taken into account for the prediction of the mean neutrino rate. The overall uncertainty on the fission fraction is assumed to be 2 %, covering the amplitude of the evolution during a full reactor cycle. Inserted in Eq.1, this leads to a 1 % uncertainty in the predicted neutrino flux. The mean fission fraction are $\alpha_{^{235}\mathrm{U}} = 92.6\,\%$, $\alpha_{^{239}\mathrm{Pu}} = 6.1\,\%$, $\alpha_{^{238}\mathrm{U}} = 0.8\,\%$ and $\alpha_{^{241}\mathrm{Pu}} = 0.5\,\%$, as expected for a highly enriched fuel.

The mean energies per fission E_k and the IBD cross-section are taken from [16] and [19] respectively. For the antineutrino fission spectra of each isotope we used the recently improved spectra from [3], converted from the ILL reference beta spectra of ^{235}U, ^{239}Pu and ^{241}Pu [20, 21]. The ^{238}U spectrum is taken from [4]. Considering the dominant contribution from ^{235}U a global 2.2 % relative uncertainty is obtained for the mean interaction rate of antineutrinos.

The distance between the reactor core centre to the detector centre was determined using a survey of the geodesic combined with information from technical drawings of the reactor building. This led to a baseline of 7.21 ± 0.11 m, corresponding to a 3.1 % uncertainty on the neutrino rate. The detector mechanical survey allowed us to compute the detector volume at 846.8 ± 7.0 L. Associated to the measurement of the target liquid mass of 739 ± 1 kg and the calculation of the ratio of free hydrogen over carbon from the known chemical composition of the liquid (H/C=1.50 ± 0.02), we computed a proton density of $5.92 \pm 0.05 \cdot 10^{28}$ proton/m^3.

To propagate the $\overline{\nu}_e$ flux from the core to the $\overline{\nu}_e$ detected rate we developed a code called NuMC, with main task to integrate numerically Eq. 1 and 2 with a Monte-Carlo method. The code firstly computes the interaction rate for a perfect detector: a given fissile isotope is drawn according to the simulated fission fraction α_k, then a $\overline{\nu}_e$ energy is drawn in the corresponding spectrum S_k, and finally a position in the core is drawn according to the simulated distribution of fissions in the core $\Psi_{\mathrm{f},k}(\overrightarrow{r_c})$. From this stage, the $\overline{\nu}_e$ is propagated in a random direction, and the length of the $\overline{\nu}_e$ path inside the detector (if any) is stored. Repeating a great number of times this procedure gives the average length of the $\overline{\nu}_e$ path inside the detector, which is l_{eff} weighted by the fission fraction. After numerical integration of the product of the spectra S_k and the cross-section $\sigma_{\overline{\nu}_e}$, the interaction rate is then obtained by applying the correct normalization factor of Eq. 1. We obtain for Osiris at 66.5 MW and 100 % of efficiency 910.8 $\overline{\nu}_\mathrm{e}$/day and 913.8 $\overline{\nu}_\mathrm{e}$/day for the two core configurations described previously, with a relative uncertainty of 4.6 % (see table I).

Then we can compute the expected number of $\overline{\nu}_\mathrm{e}$/day according to:

$$R_\nu^{\mathrm{pred}} = (R_\nu^{\mathrm{rod3}} \times T^{\mathrm{rod3}} + R_\nu^{\mathrm{rod4}} \times T^{\mathrm{rod4}}) \times \epsilon_{\mathrm{det}} \qquad (3)$$

with $R_\nu^{\mathrm{rod3}} = 910.8\,\overline{\nu}_\mathrm{e}$/day ($R_\nu^{\mathrm{rod4}} = 913.8\,\overline{\nu}_\mathrm{e}$/day) the expected number of $\overline{\nu}_e$ interactions per day at 66.5 MW with the 3$^{\mathrm{rd}}$ (4$^{\mathrm{th}}$) control rod used as the last control fuel element during the cycle. $T^{\mathrm{rod3}} = 0.32$ and $T^{\mathrm{rod4}} = 0.68$ are the relative amounts of lifetime in each configuration and ϵ_{det} the detection efficiency (see section V F 1). We obtain $R_\nu^{\mathrm{pred}} = 913\,\overline{\nu}_\mathrm{e}$/day for Osiris at 66.5 MW and 100 % of efficiency.

Source	Relative uncertainty (%)
Baseline	3.1
Fission cross-section	2.2
Thermal power	2.0
Fission fractions	1.0
Number of protons	1.2
Total	4.6

TABLE I. Summary of relative uncertainties associated to the predicted $\overline{\nu}_e$ rate, with 100 % detection efficiency.

In a second step, the NuMC code can be used as a Geant4 IBD event generator. An isotope and a fission vertex in the core are drawn, together with a vertex in the detector. This couple of vertices is stored or not according to the $1/L^2$ flux law. If this event is valid, an IBD event is generated according to the double differential IBD cross-section [19]. Finally the full kinematic information of both the positron and the neutron are saved in a data file as an input for Geant4.

We then simulate the $\overline{\nu}_e$ interactions in the detector, including scintillation and light collection on PMTs. The Geant4 output file is set to the same format as the Nucifer data. Finally processing our neutrino search algorithms on the simulated data determine the mean detection efficiency, found to be 30.3 % (see section V F 1).

IV. DETECTOR CALIBRATION

The calibration system was designed to provide an absolute energy scale to the light response of the detector and to assess the linearity and the stability of the whole

detection system. Controlled light injections allow a calibration from charge unit to photo-electrons (PE hereafter). Radioactive sources deployed temporarily in the central tube inside the detector let us to perform the final calibration from PE-scale to the MeV-scale.

The detector target vessel is equipped with 7 Teflon light diffusers, linked by optical fibres to Light-Emitting Diodes (LED) located in the electronic rack and controlled through the acquisition software. One of this LED is used to generate Single Photo-Electrons (SPEs) on the PMTs, 4 are used with different intensities to test the linearity and stability of the PMTs over their full dynamic range, and the last 2 could be used as spares. Sequences of 14 patterns, including 2 SPEs, random and multiple LED patterns, are continuously generated by the acquisition at a frequency of 5 Hz. What is referred to as a random pattern corresponds to no LED and, although periodic, is random with respect to physical triggers and therefore samples the pedestals of the digitization chain. This system allows the continuous measurement of both the pedestal and gain of each channel for each run, thanks to an automatic fit of the pedestals and of the SPE signals. Each run and channel is consequently automatically calibrated in photo-electrons, allowing a proper sum of the 16 PMT charges.

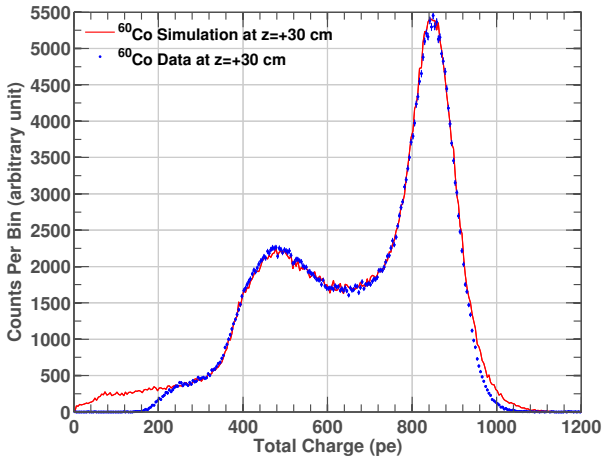

FIG. 4. Detector response to a ^{60}Co source deployed at the centre of the target vessel compared to the detector response simulation. No threshold was applied in the simulation, leading to the low energy discrepancy. For all calibrations, the hardware threshold is different from the data taking threshold, adapted to the energy range and the trigger rate.

The detector response to multiple LED patterns compared to single LED pattern is linear within 1 %, showing no drift at higher intensities and the uncertainty on pedestals is below 1 %. On a run-to-run basis the variance of the fitted SPE is typically 2.5 % with perfect Gaussian shape. On longer time scales the gains and the linearity of the response to LED patterns have shown remarkable stability. Larger drifts due to temperature changes in the electronic rack are observed on the absolute value of pedestals and LED signals. They are correlated on all channels and corrected for each run.

Small encapsulated radioactive sources can be deployed inside a vertical tube along the target central axis. Three gamma-emitting sources of few kBq activity have been used: a ^{137}Cs source with one 661 keV γ-ray, a ^{60}Co source with two γ-rays of 1173 and 1332 keV in coincidence, and a ^{22}Na source with one γ-ray of 1274 keV in coincidence with two γ-rays of 511 keV coming from the annihilation of the positron. We also used a neutron source of ^{241}Am-Be, emitting a neutron in coincidence with a γ-ray of 4.4 MeV for $\sim$ 75 % of the events. The activity of the ^{241}Am reaches few MBq, leading to only $\sim$ 30 Hz of neutrons. This source is mainly used to test our analysis procedure for searching correlated pairs of events and study the neutron physics (capture time and detection efficiency).

These calibration sources were inserted at different elevation levels in the central vertical tube and used to tune a Geant4.9.4-based simulation (in PE units) to reproduce the measurements. A good agreement between experimental and simulated spectra could be achieved for most positions (see Fig. 4). However at the highest source location, close to the acrylic buffer coupling to the PMTs, sizeable deviations from the data still remain, likely due to the difficulty of properly simulating light collection for events interacting close to the PMTs.

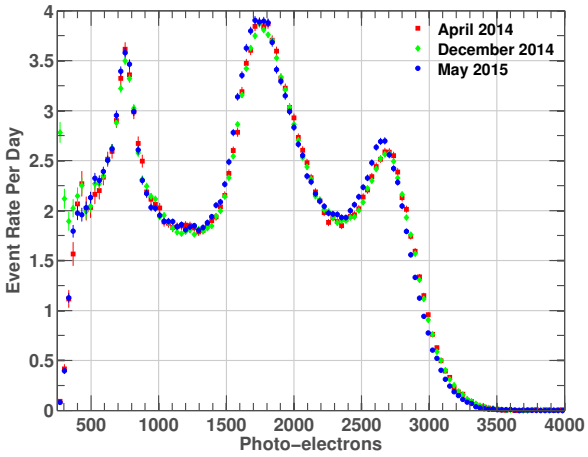

FIG. 5. Detector response to a AmBe source deployed at the centre of the target vessel at three different periods from April 2014 to May 2015. The right peak corresponds to the neutron capture on Gd at 8 MeV. The middle peak comes from the reaction of α particle on ^{9}Be, leading to the emission of a 4.4 MeV gamma ray and a fast neutron, and depositing a mean energy equivalent to an electron of 5.5 MeV. Due to the quenching effect, neutron induced nucleus recoils do not produce as much light as an electron of the same energy. The left peak corresponds to neutron capture on hydrogen, with the emission of a unique 2.2 MeV gamma ray.

A global calibration factor of $\sim$ 340 PE/MeV has been obtained with the 4 sources of calibration. The uncer-

tainty on this factor is latter included in the global energy scale uncertainty (see section V F 2). With a source at the centre of the target we measure an intrinsic energy resolution of 10 % at 1 MeV. This value increases to about 20 % for vertices uniformly distributed in the target volume because of the light absorption on the Teflon-coated walls of detector target. Figure 5 illustrates the very good stability of the detector response to the AmBe source along the whole data taking period.

V. DATA ANALYSIS

A. Data sample

The signature of IBD events consists in a delayed coincidence starting by a prompt positron energy deposition, E_{prompt}, followed by a neutron induced energy deposition, E_{delay}, due to the de-excitation gamma ray(s) after its capture on H or Gd within Δt_{e^+n}. The principle of the analysis is to compare the number of $\overline{\nu}_e$ detected to the prediction based on the reactor data and reactor core simulations. The challenge consists in the statistical separation of IBD events with respect to backgrounds induced either by random coincidences of single events or by correlated coincidences originating from air showers and possibly from reactor core radiations.

At Osiris, a running cycle is nominally operating for three weeks with the reactor ON followed by a week of reactor OFF period. The results described in this paper are based on 10 cycles accumulated from June 2014 to July 2015, after the Nucifer upgrades. Power transients at the beginning of each cycle (few hours) are discarded from the data sample due to the difficulty to assess the thermal power of the reactor during this phase. Therefore our sample consists of 200 days of reactor ON at full power. Nevertheless the lifetime of the Nucifer data acquisition is only 145 days. A loss of 5 days is due to the 100 µs veto of the acquisition after each tagged muons. The remaining inefficiency is dominated by unattended periods of data taking during which the synchronization of the different electronics readout buffers of the data acquisition system was lost. The bad runs are rejected by an automatic off-line quality check. The total of reactor OFF time is 153 days including inter-cycles periods and longer shutdowns for reactor maintenance. The Nucifer lifetime during this OFF period is 106 days. We thus obtain an overall data taking efficiency of 70 %. It is worth noting that this efficiency could easily be improved to more than 90 % by implementing an automatic recovery procedure to handle data acquisition system failures.

In the following, event rates are reported with statistical uncertainties only. Systematic uncertainties are gathered in the predicted neutrino rate uncertainty.

B. Neutrino candidate selection

The analysis cuts are optimized to reach the smallest relative uncertainty on the detected neutrino rate [22] in the severe background conditions described in the sections V C and V D 1.

From the prediction of the emitted neutrino spectra and the kinematics of the IBD reaction the expected range of E_{prompt} is 1.022 MeV to about 7 MeV. Given the steep increase of background at low energy, a 2 MeV threshold is used, well above the hardware threshold, giving negligible trigger inefficiency. Then the maximum prompt energy is set at 7.1 MeV above which the remaining IBD positron induced rate is negligible.

The delayed event energy is not related to the incident neutrino energy. Its associated 8 MeV γ-cascade from the neutron capture on a Gd nucleus is used to efficiently discriminate the neutrino signal against lower-energy background events. However in a meter-scale detector like Nucifer one has to accommodate for important energy leakages shifting most of the delayed events into lower energy bins. Indeed, the most probable energy deposited in Nucifer after a neutron capture on Gd is about 4.5 MeV only. Again the limitation to open the E_{delay} range towards lower energies is the steep increase of the accidental background. We thus optimized the delayed energy range to $4.2\,\text{MeV} < E_{delay} < 9.6\,\text{MeV}$.

The coincidence time window Δt_{e^+n} is limited to 40 µs after each prompt candidate. This duration corresponds to only twice the expected neutron capture mean parameter, τ_n. This upper limit is a compromise between the rejection of about 15 % of the neutrino signal and the mitigation of the accidental background rate, growing linearly with the prompt-delayed gate duration. Furthermore the delayed event time must also be separated from the prompt energy deposition by more than 6 µs due to the dead time of the QDC needed to process the PMT signals after each trigger.

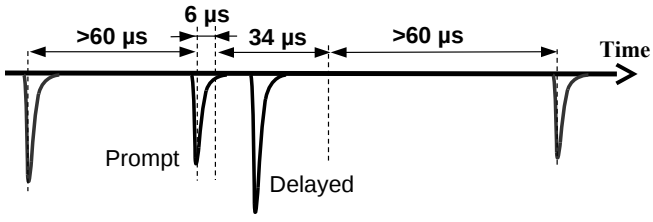

FIG. 6. Time selection of neutrino candidates. The prompt event must be separated by more than 100 µs with respect to any muon veto trigger.

All events occurring less than 100 µs after a muon event are overridden. A muon event is defined either as a muon veto trigger or as the saturation of at least 15 PMTs. Finally an isolation selection criteria, called multiplicity cut, is applied to all prompt-delayed pairs. It imposes that no energy deposition occurs either 60 µs before the prompt event or 60 µs after the end of the delayed gate

(see Fig. 6). This cut rejects cosmic-ray-induced background with more than two particles in the same shower. All selection criteria are summarized in table II.

Criterion	Applied cut
Prompt event	$2.0\,\text{MeV} < \text{E}_{\text{prompt}} < 7.1\,\text{MeV}$
Delayed event	$4.2\,\text{MeV} < \text{E}_{\text{delay}} < 9.6\,\text{MeV}$
Time selection	$6\,\mu\text{s} < \Delta t_{e+n} < 40\,\mu\text{s}$
Multiplicity	No trigger 60 µs before prompt event
	No trigger 60 µs after delayed gate
Muon veto	100 µs

TABLE II. Summary of neutrino selection criteria.

In the following we will focus on the accidental and the correlated backgrounds. Indeed the very short baseline coupled with the shallow depth of the experiment imply that these backgrounds make much larger contributions than the expected neutrino signal does. Therefore an accurate determination of these spurious event rates is the main challenge of the Nucifer analysis.

C. Accidental background

When the reactor is OFF, the trigger rate is dominated by muons events ($\sim$ 350 Hz in the muon veto), and once muons have been excluded, by low energy natural radioactivity decays (65.7 Hz above 2 MeV) whose energy spectrum is shown in red on figure 7. Beyond the rapid decrease of the energy spectrum after the threshold at about 500 pe, one can see a small peak at 2.6 MeV (880 pe) corresponding to the highest natural gamma ray of ^{208}Tl decay (^{60}Co in the tank stainless steel is less than 12 mBq/kg from a sample measurement and therefore negligible), and an ankle near 8 MeV (2700 pe) attributed to natural neutron capture. The tail at high energy is attributed to the contamination by events induced by atmospheric showers in the vicinity to the detector that do not trigger the muon veto nor saturate at least 15 PMTs.

When the reactor is ON the shape is different and the total event rate increase (177.1 Hz above 2 MeV). The associated spectrum (blue curve on figure 7) shows a rather smooth shape up to about 10 MeV. Such high-energy depositions are attributed to neutron radiative captures on metallic structures and concrete wall components, such as iron, nickel or aluminium, occurring in the vicinity of the detector and emitting high-energy γ that can pass through the shielding and finally reach the detector target. The bump around 6 MeV (2000 pe) comes from the ^{16}N decay gamma rays in the deactivation circuit (see section II B).

As a consequence both the prompt and the delayed energy windows are affected by the reactor induced events, which has a strong consequence: the accidental background event rate scales quadratically (instead of linearly) with the gamma-ray flux ϕ_γ, proportional to the reactor power. A crude model of the neutrino-like event rate is $\tau_{\bar{\nu}} = \tau_{\text{prompt}} \times \tau_{\text{delay}} \times \Delta t_{e+n}$. Both prompt and delayed event rates are dominated by backgrounds events, and if both are affected by reactor induced events we get $\tau_{\text{prompt}} \propto \phi_\gamma$, $\tau_{\text{delay}} \propto \phi_\gamma$ and finally $\tau_{\bar{\nu}} \propto \phi_\gamma^2$. Adding lead shielding could therefore reduce greatly the accidental background, but the mass limit on the Osiris floor has already been reached.

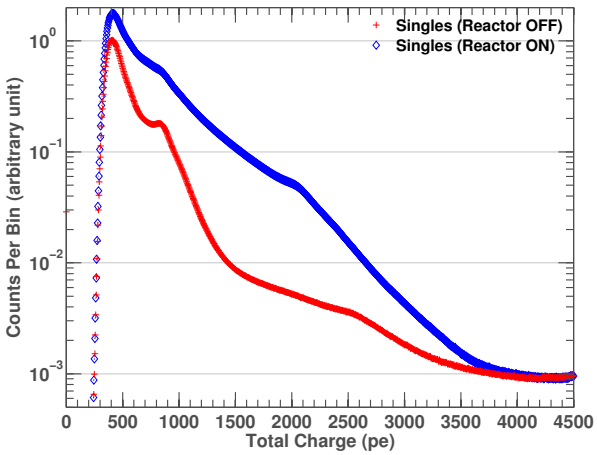

FIG. 7. Energy spectrum of the single event rate at reactor full power and during reactor OFF combined periods.

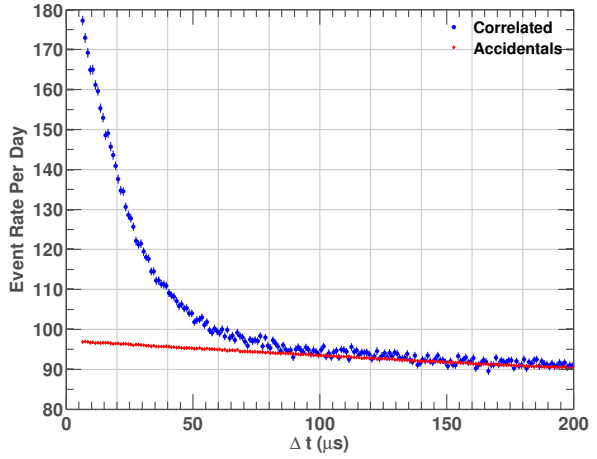

FIG. 8. Distribution of the time difference between prompt and delayed events for all correlated candidates (blue) and for the accidentals (red). The data sample accumulates 10 reactor cycles.

Nevertheless this high accidental background level can be accurately measured by analysing off-time coincidences. For each delayed-like event, all past prompt events in the run are shifted in time up to 100 times by steps of 1 ms, until the next past prompt is repositioned less than 1 ms before the current delayed event. If the so-

formed virtual pair complies with the neutrino selection cuts, it is counted as an accidental event. This method allows to measure the accidental background 100 times for each run, in the exact same conditions of data taking, and consequently this background is measured with a negligible statistical uncertainty. Unfortunately, this method limits the impact of the high accidental event rate on the final statistical uncertainty only for one of the two terms of the subtraction (see also table V). Noting N the event number, Δt the acquisition time, and τ the events rates, the correlated event rate error is:

$$\delta_{\rm corr} = \sqrt{\left(\frac{\sqrt{\rm N_{candidate}}}{\Delta t}\right)^2 + \left(\frac{\sqrt{\rm N_{acc}}}{100\times\Delta t}\right)^2} \quad (4)$$

$$= \sqrt{\frac{\tau_{\rm corr}+\tau_{\rm acc}}{\Delta t} + \frac{1}{100}\frac{\tau_{\rm acc}}{\Delta t}} \sim \sqrt{\frac{\tau_{\rm acc}}{\Delta t}} \quad (5)$$

where we see that if the 100 shifted gates allow to neglect the uncertainty brought by the accidental events subtraction, the final uncertainty is still dominated by the accidental event rate, as $\tau_{\rm corr} \ll \tau_{\rm acc}$.

Furthermore, great care is brought into the evaluation of the efficiencies of the multiplicity cut and muon veto as they slightly differ between the searches for correlated pairs and accidental pairs. A cross-check of our accurate determination of accidental rate is illustrated in figure 8 where the number of measured correlated and accidental pairs is plotted as a function of Δt_{e^+n} for a same sample of reactor ON data. The correlated events clearly show up as an exponential curve on top of the accidental background with a decay time corresponding to the n-capture time $\tau_n \simeq 20\,\mu$s. The distribution of pure accidentals, determined with the off-time prompt events, perfectly matches the correlated curve for $\Delta t_{e^+n} \gg \tau_n$.

Within the selection cuts, summarized in table II, the average accidental rates measured for the whole data sample are 69.1 ± 0.1 events/day when the reactor is OFF and 3476.3 ± 0.7 events/day when the reactor is ON (at full power), respectively. Therefore this dominating background is 11.9 times larger than the expected neutrino rate. In the following all quoted rates will be corrected for their associated accidental rates.

D. Cosmic induced background

1. *Origin and rejection*

The correlated events above the accidentals events in figure 8 are still not a pure sample of neutrinos. At the shallow depth of Nucifer (12 mwe), the cosmic-ray particles induce correlated backgrounds through the multiple secondary particles produced in the air shower and also through their interaction in the ceilings above the detector (especially for the penetrating muons). It is worth noting that the overburden above the detector is not sufficient to stop all the hadronic component of the atmospheric cascades, leaving the possibility for some fast neutrons to reach the liquid scintillator.

The most probable candidates at the origin of cosmic induced correlated backgrounds are fast neutrons from a air shower or created by an inelastic muon interaction (spallation) in materials above or nearby the detector. First, a fast neutron can scatter off nuclei in the detector target, mimicking prompt-like energy deposition, and later be captured on Gd providing a delayed-like energy deposition with a similar prompt-delayed time correlation than expected for neutrinos. Second, two neutrons from the same shower can be captured successively in the detector, after some diffusion in the liquid or in the shielding. As the gamma collection efficiency after neutron capture on Gd is poor in Nucifer, the first neutron capture energy deposit is very likely to be in the prompt energy window. Third, fast neutron can also produce high energy gamma rays by inelastic scattering on nuclei, such as the $^{12}{\rm C}(n,n')\gamma$ reaction producing 4.4 MeV gamma rays on the first nuclear excitation level. The gamma interaction would of course mimic the prompt event and the later neutron capture the delayed event.

Fortunately, this last background process whose signature is very similar to the IBD can be safely neglected with respect to the first process (elastic scattering mimicking the prompt event): the $^{12}{\rm C}(n,n')\gamma$ cross-section is always well below both the hydrogen and the carbon elastic scattering cross-section, by a factor 5 to 10 each depending on the energy [14].

Highly energetic muons may also create long-lived β-n emitters such as ^{9}Li or ^{8}He when interacting with Carbon nuclei belonging to the scintillator molecules. The rate of β-n events from ^{9}Li or ^{8}He decays was estimated to 2.7 events/day by scaling the measurement of the Double Chooz experiment to the Nucifer shallow depth [23]. We compared this estimation with our analysis of events following high energetic muon depositions in the detector target at time differences compatible with the decay time of ^{9}Li (~ 270 ms). The muons showering inside the Nucifer target could be tagged by lowering the gain of one target PMT. No ^{9}Li induced background candidate was clearly identified. In consequence an upper limit of less than 12 events/day at 95 % C.L. was set [22]. Therefore this background can be considered as negligible with respect to the total rate of correlated events.

As the muons entering the detector are tagged by the veto system surrounding the detector, most of the secondary products of the muon interactions are removed from the data sample by discarding events occurring within 0.1 ms after each recorded muon. A further background reduction is provided by the multiplicity cut, rejecting most of the neutron induced background. *In fine*, the remaining contribution is subtracted using reactor-OFF data, representing about 45 % of the data taking time. Averaged over the whole reactor OFF data, a correlated event rate of $1145.4 \pm 3.4 \pm 2.5$ events/day is measured, i.e. 3.9 times higher than the expected neutrino rate.

2. Stability and correction

Last but not least, before subtracting this correlated background to obtain the experimental neutrino rate, one has to assess its stability over the time scale of a reactor cycle. Indeed the correlated background is found to vary over time and consequently an extra probe of the correlated background must be defined to monitor and subtract properly the actual background rate during each reactor ON period.

A probe is the muon rate, accurately recorded for each run. Here we define a muon trigger as the combination of a signal in the muon veto and the saturation of at least 15 PMTs. This definition reduces the sensitivity to high-energy γ that can trigger the muon veto when the reactor is ON and allows a reliable comparison between reactor ON/OFF muon rates. Table V shows that indeed the muon rates measured this way for the averaged reactor ON and OFF periods are very close, 110.6 and 110.1 Hz respectively. The main origin of this variation of muon rates is the natural variation of the atmospheric pressure: we could check that the remaining 0.5 Hz difference is coherent with the different mean atmospheric pressures recorded for the two averaged periods (998 and 1002 hPa) and the observed correlation of -0.117 ± 0.008 Hz/hPa. Figure 9 (top) shows that the variations of the correlated event rate among various reactor OFF periods are very well correlated with the muon rate. Once the correlation with pressure is removed no sizeable dependence on temperature or humidity was found.

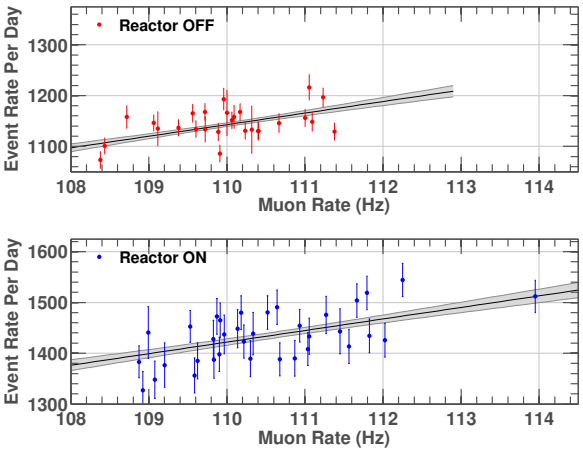

FIG. 9. Correlation between the rate of correlated background measured with the reactor ON/OFF and the rate of triggers tagged as muons. The slope is $-22.8 \pm 5.0\,\text{event day}^{-1}\,\text{Hz}^{-1}$.

At first glance one would expect a zero intercept and a relative change of the muon rate equal to the relative change of the correlated background. This is clearly not observed. More complex physics must be brought into play to explain the true dependence, probably due to the fact that the tagged muons saturating the detector are not fully representative of those inducing the correlated background (coming from interactions outside the detector). Hence a linear fit is considered more as an effective model within the limited range of variation of the muon rate. What matters for the subtraction is that the same correlation applies on the reactor-OFF data. This is indeed the case as shown in figure 9 (bottom) where the muon rate dependence measured for reactor OFF periods is in very good agreement with the one for reactor ON data. Hence the subtraction of the correlated background is performed the following way:

- The absolute correlated event rate per day is given by the reactor OFF data. The global correlation with the muon rate is determined as accurately as possible, combining reactor ON and OFF data to constrain the muon rate dependence. The final error band is shown as a grey shaded area in figure 9.
- The muon rate is measured for each reactor ON period.
- The corresponding correlated background and its associated uncertainty is deduced from the correlation with the muon rate. This reactor OFF contribution is subtracted from the total rate of correlated events measured reactor ON.

As the difference between average reactor ON and OFF muon rate is only 0.5 Hz and the slope of the correction is $-22.8 \pm 5.0\,\text{event day}^{-1}\,\text{Hz}^{-1}$, the correction reaches 11.4 event/day and introduces a small systematic uncertainty on the final neutrino rate of 2.5 event/day. When the data sample is separated in shorter time period, this error increases for each single data point, depending on the actual muon rate.

E. Reactor induced correlated background

1. Neutron induced correlated background

Due to the proximity of the detector with the reactor, fast neutrons generated by the core could penetrate the polyethylene shielding producing additional correlated background. This kind of events could be even more problematic with respect to the cosmic ray induced neutrons since the associated background cannot be subtracted using reactor OFF data. We consider here only one correlated background process: neutron elastic scattering on nuclei mimicking the prompt event. Even if a fission generates several fast neutrons, it is extremely unlikely that 2 neutrons from the same fission scatter off nuclei in the (small) Nucifer detector located several meters away. We also consider that the inelastic scattering on nuclei process is negligible with respect to elastic neutron scattering (see section V D 1).

In order to check if a background contribution remains on top on the reactor OFF data, we exploit the Pulse Shape Discrimination (PSD) capability of the Nucifer liquid scintillator. Aside the total charge recorded for each

trigger ($Q_{\rm tot}$), a late charge is also recorded ($Q_{\rm tail}$, see II). The distribution of the ratio $Q_{\rm tail}/Q_{\rm tot}$ of all prompt candidates is displayed in figure 10 for reactor ON and OFF data. As expected, two peaks emerge, one centred at $Q_{\rm tail}/Q_{\rm tot} \simeq 0.24$ corresponding to electron recoil and another one centred at a higher value, 0.29, corresponding to nucleus recoils induced by fast neutrons. In the comparison between the ON and OFF PSD spectra the neutrino signal clearly shows up as a Gaussian distribution centred at 0.24, as expected from the positron (electron-like) recoil. For large $Q_{\rm tail}/Q_{\rm tot}$ values corresponding to nucleus recoils, both spectra overlap and demonstrate that the background subtraction is well under control.

Adjusting each curve with the sum of two Gaussians, the compatibility of the nucleus recoil peaks in our errors bars is confirmed. However, the reactor ON peak exhibits 18 more events than the reactor OFF peak, in the 0.3 to 0.4 $Q_{\rm tail}/Q_{\rm tot}$ range. We conclude that the reactor induced correlated event rate is 0 ± 18 events/day, and add this as an additional systematic uncertainty to the final neutrino rate measurement. It is worth noting that the delayed gate used to record $Q_{\rm tail}$ has suffered from an electronic jitter during the major part of our data taking, not constant in time, before we could identify and correct the defective gate generator. This electronic jitter is our best hypothesis to explain the mismatch between the nuclei recoil peaks ON and OFF.

To better constrain the neutron induced correlated background, we performed a complete TRIPOLI-4® simulation. The starting point is a core simulation that samples outgoing fast neutrons (> 2 MeV) at the surface of the core. These particles are then used as a source for a second simulation that propagates the neutrons to the Nucifer target volume, using sophisticated variance reduction techniques to push the particles through the thick absorbing media. In particular, we used INIPOND, a special built-in module of TRIPOLI-4® based on the exponential transform method [24]. This exponential biasing is performed using an importance map which provides information on the probability, for each point of the phase space, for a particle to reach the detector. It is first calculated with a simplified deterministic solver and then adjusted by hand. The code uses this information to adjust the propagation of the neutrons along the path to the detector, thereby reducing the variance of the calculated observables without introducing any bias.

We found that the neutron elastic scattering rate on hydrogen in the whole Nucifer target volume is $4 \cdot 10^{-5}$ event/day for neutrons with energies higher than 2 MeV, corresponding to an attenuation of the order of 10^{-27}. This rate is a large overestimation because we neglected the real energy transfer, the quenching and the prompt-delayed coincidence, considering each neutron elastic scattering on hydrogen as a background event satisfying all our selection cuts. The statistical uncertainty reported by TRIPOLI-4® is at the percent level but large systematic uncertainties have to be considered, simply by the propagation of errors on initial parameters (cross-section, composition...) on such enormous attenuation. The results should therefore be considered as an order of magnitude estimate. Despite the large uncertainty, our conservative approach ensures that the neutron induced correlated background is negligible.

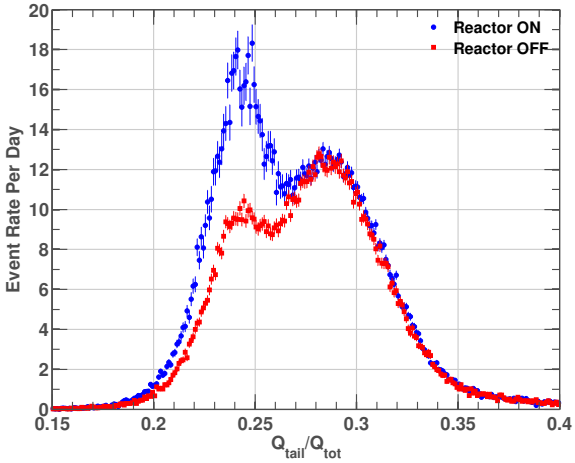

FIG. 10. Distributions of the PSD parameter $Q_{\rm tail}/Q_{\rm tot}$ for reactor OFF (squares) and reactor ON data (circles), obtained after subtraction of the accidental background and correction for the cosmogenic rate modulation.

Note that the separation between proton and electron-like recoils could in principle be used for further rejection of the correlated background. A cut $Q_{\rm tail}/Q_{\rm tot} < 0.27$ would remove about 2/3 of the reactor OFF background. However this criterion is not currently in force in our analysis since the rather poor separation between the 2 peaks implies a potentially large migration of events from both sides of the cut should slight drifts in the pulse integration occur. The application of this PSD cut would thus lead to an extra systematic uncertainty whereas our dominant background is coming from accidental coincidences.

2. *Gamma induced correlated background*

We also considered the gamma correlated background: a gamma ray with sufficiently high energy could excite a nucleus by inelastic scattering, and if excited above the neutron separation energy the nucleus could emit a neutron. This process demands very energetic gamma ray since the typical neutron separation energy is above 10 MeV for stable light nuclei (^{12}C, ^{16}O, ^{56}Fe) and in the 6–8 MeV range for heavy nuclei (Pb, Gd), with strong effects of neutron number parity (several MeV) so that some rare stable nuclei have lower neutron energy separation (e.g. 4.1 MeV for ^{17}O, 4.9 MeV for ^{13}C).

If the gamma energy is high enough, the neutron could be fast and create correlated background as in the previous scenario. But up to 6 MeV proton recoils produce

3 times less light than electron recoil due to quenching [25, 26], therefore the neutron should have at least 6 MeV to enter our prompt energy window. Adding this energy to the neutron separation energy demands an initial gamma energy higher than what is observed in the Nucifer spectrum (see Fig. 7).

Another possibility is the creation of a low energy neutron, the remaining energy being left to the gamma ray. If both particles enter the detector and are absorbed, the gamma ray can create the prompt event and the neutron capture the delayed event, with a time correlation identical to neutrino events. To enter the prompt energy windows, the gamma ray must have kept at least 2 MeV, and because the neutron would have low energy, the probability to go through the polyethylene shielding without being captured on Boron would be negligible. Therefore the initial inelastic scattering should take place in the tank, on some odd neutron number light nuclei. But such nuclei have low natural concentration (percent or less), at such energy the cross-section of (γ, n) reaction ($2.0 \cdot 10^{-4}$ barn for ^{13}C at 7 MeV [27, 28]) is much lower than Compton scattering cross-section ($3.96 \cdot 10^{-1}$ barn for C at 7 MeV [29]) and the interaction rate of high energy gamma in Nucifer is low enough (about 0.5 Hz above 7 MeV) so that this process can be safely neglected.

F. Detection efficiency and associated systematics

1. *Detection efficiency*

As explained in section II, a dedicated software package generates a set of simulated $\overline{\nu}_e$ events in the same format than the data. To determine the detection efficiency we apply the exact same analysis chain and compute the amount of rejected events. Since the path lengths of γ-rays and neutrons in the liquid scintillator (~ 20 cm) are not negligible with respect to the size of the detector target (1.2 m diameter), edge effects induce sizeable correlations between the analysis selection criteria. In consequence the total detection efficiency is not the simple product of the efficiencies of all single cuts. It is defined as the ratio of the number of simulated events passing all the analysis selection criteria to the total number of neutrino vertices generated in the liquid scintillator. Using the selection procedure described previously the global detection efficiency is found to be 30.3 %.

As shown on table III, taking each cut individually the selection of the delayed energy deposition (47.9 % efficiency) is the selection criteria that degrades most the efficiency. This is due to the lack of containment of the multiple high-energy γ-rays released after the neutron capture on Gd in the small, 619.2 mm in radius and 704.9 mm in height, detector target. The time selection is the next limiting cut (63.1 %), rejecting the same amount of event below and after the gate, and finally the low energy cut at 2 MeV has a rather strong influence on the prompt event selection (76.6 %). According to the simulation, IBD neutrons are captured mostly by the Gadolinium (85 %), then by the Hydrogen (11 %), the Boron (2 %, in the polyethylene shielding) and the remaining by the steel components. 7.2 % of IBD neutrons are captured outside the target.

The efficiency of the multiplicity cut is computed by counting the number of diode triggers with and without applying this cut. Because of their different single rates reactor ON and OFF have different multiplicity efficiencies found to be 0.974 and 0.990, respectively. They both have a negligible associated systematic uncertainty and the correction is applied during the data analysis. Finally the 3.9 % dead-time induced by the μ-veto is independently computed with negligible uncertainty from the μ triggers, taking in account overlaps between veto gates. This veto time is subtracted from the total live-time of the analysed runs.

Selection cut	Efficiency
$6\,\mu s < \Delta t < 40\,\mu s$	63.1 %
$2.0\,MeV < E_{prompt} < 7.1\,MeV$	76.6 %
$4.2\,MeV < E_{delay} < 9.6\,MeV$	47.9 %
ϵ_{det}	30.3 %
	Dead-time
Multiplicity ON	2.6 %
Multiplicity OFF	1.0 %
Muon veto	3.9 %

TABLE III. Detection efficiency or induced dead-time of the selection cuts. As explained in the text the total efficiency is not the simple product of cut efficiencies because of correlations between the cuts.

2. *Systematic uncertainties*

The uncertainty on the energy scale is determined by comparing the delayed spectrum of correlated pairs in the reactor OFF data (Fig. 11) with the Geant4.9.4 simulation of thermal neutron uniformly distributed inside the lead shielding, once the Geant4 simulation has been tuned to reproduce at best the source spectra at different positions. This set of data was chosen because it is independent from the calibration data, it shows several spectral features among the whole energy range and the energy depositions are uniformly distributed in the whole target volume, as expected from neutrino candidates. Note that the source in the simulation, uniformly distributed thermal neutron, is a crude approximation of the natural neutron flux at shallow depth. But the simulation is not intended to reproduce exactly the measured spectrum, particularly the relative weight of the energy features, but to allow the comparison of the position of these features to establish the energy scale uncertainties.

The main features of the energy spectrum (n-capture peak on H at 750 PE, a middle bump at about 1700 PE

and a high energy edge of n-capture on Gd) are clearly visible for both data and simulation. The $n(\mathrm{H,D})\gamma$ peak position, the transition between the two plateaux at 1200 PE and 2200 PE, and the $n(\mathrm{Gd,Gd})\gamma$ shoulder position are fitted on both data and MC. The largest difference is found to be 2.5 % and is taken as a safe estimate of the energy scale uncertainty. To determine the efficiency uncertainty due to energy scale, we repeated our analysis of the simulated neutrino data set 1000 times with a variation of energy cuts. At the beginning of each analysis, a factor is shot in a Gaussian distribution of relative standard deviation 2.5 %, and each energy cut is multiplied by this factor. The distribution of all the neutrino rates found is a Gaussian which standard relative deviation, 1.0 %, is the uncertainty on efficiency due to energy scale.

Nucifer is made of a unique volume of liquid scintillator enclosed in a stainless steel tank. Therefore, neutrino interaction outside the target leading to light production can only happen in the acrylic buffer, with the positron depositing at least 2 MeV in the liquid scintillator. Thus only the first centimetres of the buffer are concerned. We simulated IBD events uniformly distributed in the buffer and found that less than 0.15 % of such events pass the analysis cuts, a negligible quantity (less than 0.5 event/day).

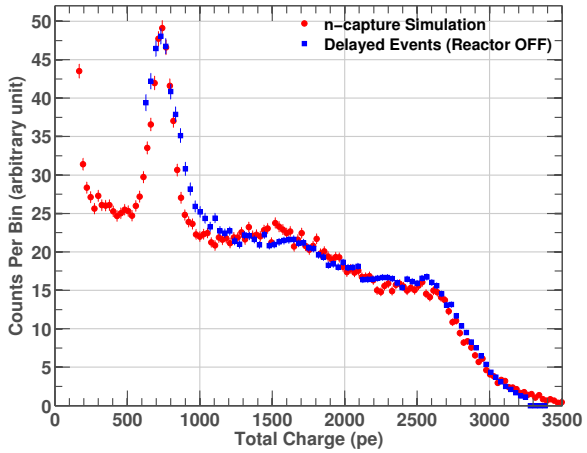

FIG. 11. Photo-electron spectrum of delayed energy events during a reactor OFF run compared to a Geant4.9.4 simulation of low energy neutrons uniformly distributed in a sphere of 2 m radius centred on the target vessel. The n-capture peak at 750 PE (2.2 MeV) is prominent because of the numerous captures occurring in the polyethylene shielding around the target. The data threshold comes from the software analysis, thus not affecting the $n(\mathrm{H,D})\gamma$ peak, while the simulation has no threshold.

The uncertainty associated to the time selection criteria is determined by comparing Geant4.9.4, Geant4.9.4 with the addition of a module dedicated to thermal neutron physics [30] and TRIPOLI-4® simulations, using different description of low energy neutron physics. We find a 1.7 % error from the dispersion of these 3 simulation results, taking as central value the Geant4.9.4 simulation with the additional thermal neutron module. We also add a 1 % uncertainty on the efficiency due to the modelling of the gamma cascade following a neutron capture on Gd, by comparing the results of our 3 simulations.

The measurement of the neutron mean capture time with the AmBe source or the reactor OFF correlated events can not be directly used because the initial energy and spatial distributions of the neutrons are different. Indeed, the thermalization phase of neutrons from IBD is not detectable due to our electronic dead time (6 µs), while the $\Delta t_{\gamma-n}$ distribution of AmBe events shows a peak at 10 µs, then an exponential decay with a shorter parameter of 17.6 ± 1.2 µs for a source at the centre of the detector. Neutrons from a ^{252}Cf source would suffer from the same problem.

Finally, the efficiency and the associated uncertainty are 30.3 ± 2.2 % (see table IV), but here 2.2 % is an absolute uncertainty on the efficiency of 30.3 %. Therefore, the relative uncertainty on efficiency is 2.2 %/30.3 % = 7.2 %, and the predicted neutrino detection rate is $R_\nu^{\mathrm{pred}} = 913\,\overline{\nu}_\mathrm{e}/\mathrm{day} \times 30.3 \pm 2.2\,\% = 277 \pm 23\,\overline{\nu}_\mathrm{e}/\mathrm{day}$ (see section for the predicted $\overline{\nu}_e$ interaction rate III B).

Source	Uncertainty
Time cut	1.7 %
Energy scale	1.0 %
Gd(n,γ) cascade	1.0 %
IBD in buffer	0.2 %
Absolute efficiency uncertainty	2.2 %
Relative efficiency uncertainty	7.2 %
$\overline{\nu}_e$ interaction rate	4.6 %
Total prediction uncertainty	8.5 %

TABLE IV. Breakdown of the detection efficiency systematic uncertainties, and final prediction uncertainty. $\overline{\nu}_e$ interaction rate uncertainties are listed on table I.

VI. RESULTS

The distribution of neutrino events is obtained after subtracting the accidental background and the correlated background from the raw number of candidate pairs. In Fig. 12 the spectrum of the prompt-delayed time differences is found to be in agreement with a pure exponential curve with a decay time of 19.7 ± 0.9 µs, compatible with the decay time expected from the simulation.

We can use this curve to set a constraint on possible residual accidental background that would essentially show up as an extra offset. Adding this free parameter in the fit the value converges on $8 \cdot 10^{-3}$ with an uncertainty of $6.6 \cdot 10^{-2}$ that makes it perfectly compatible with zero. Integrating this error bar between 6 and 40 µs we obtain a

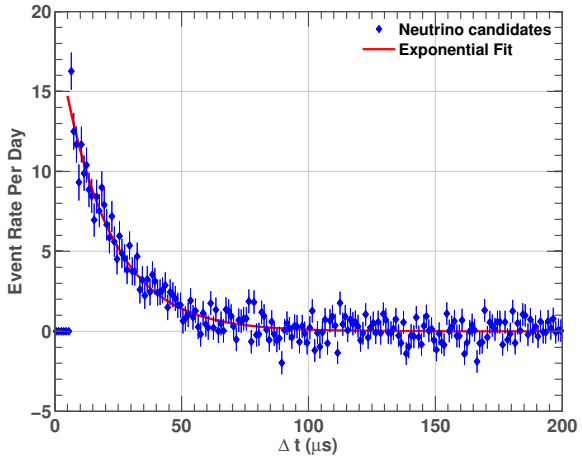

FIG. 12. Distribution of the prompt-delayed time differences for all neutrino candidates after background subtraction. The spectrum of the prompt-delayed time differences is found to be compatible with a pure exponential curve with a decay time of $19.7 \pm 0.9\,\mu s$, in agreement with the expected value.

possible "accidental-like" contribution of 2.3 events/day. This corresponds to only 0.07 % of the measured accidental rate and thus demonstrates the good quality of the subtraction.

From the number of entries we get a total of 40 760 $\overline{\nu}_e$ detected in Nucifer, corresponding to a mean rate of $R_\nu^{obs} = 281 \pm 7(stat) \pm 18(syst)\,\overline{\nu}_e$/day. The expected detected neutrino rate is $R_\nu^{pred} = 277 \pm 23\,\overline{\nu}_e$/day and therefore $R_\nu^{obs}/R_\nu^{pred} = 1.014 \pm 0.108$.

Single rates (Hz)	ON	OFF
μ veto	344.3	376.4
μ veto & Saturation	110.6	110.1
Singles	177.1	65.7
Prompt singles	75.4	16.1
Delayed singles	15.7	1.6
Pairs (/day)	ON	OFF
Candidates	4903 ± 7	1223.5 ± 3.4
Accidentals	3476.3 ± 0.7	69.1 ± 0.1
Correlated	$1426 \pm 7 \pm 18$	$1145.4 \pm 3.4 \pm 2.5$
R_ν^{obs}	$281 \pm 7(stat) \pm 18(syst)\,\overline{\nu}_e$/day	
R_ν^{pred}	$277 \pm 23\,\overline{\nu}_e$/day	

TABLE V. Summary of relevant rates for reactor ON and OFF periods. Note that the number of observed neutrinos R_ν^{obs} is not directly the ON-OFF difference of correlated events, as correction for the multiplicity cut and for the different mean muon rates have been applied. Errors reported on candidate and accidental event rates are statistical only, while errors on correlated rates also show systematic uncertainties due to background subtraction. All other systematic uncertainties are applied on the predicted rate.

All relevant rate, averaged over the full reactor ON and OFF data sets, are summarized in table V. The time evolution of the detected neutrino rate is shown in figure 13 where the data are grouped in periods of about 5 days. The alternation of ON-OFF periods is clearly visible. The null rate corresponds to the correlated background event rate averaged over the full reactor OFF data.

The statistical accuracy per 5 days of data taking is about 11 %. As expected the intrinsic statistical accuracy of the daily neutrino rate is decreased by a factor 4 due to the total background contribution being 16 times higher than the signal (11.9 from the accidentals and 3.9 from the cosmic-ray-induced correlated events). As illustrated in figure 15 the isotopic composition of the Osiris reactor is quite stable in nominal operation. Consequently only sub-percent variation of the emitted $\overline{\nu}_e$ flux are expected between the beginning and the end of a cycle [31]. The observation of this Osiris intra-cycle rate evolution is clearly out of reach of a Nucifer-like detector.

The current statistical sample accumulated by the Nucifer experiment provides a modest sensitivity to test the Reactor Antineutrino Anomaly. The current 7.2 % large uncertainty on the absolute predicted normalization factor prevents any strong conclusion in favour or against the averaged R_ν^{obs}/R_ν^{pred} discrepancy, as shown by figure 14. Improving these results is beyond the scope of this publication. A significant work will be necessary to refine the prediction of the expected neutrino rate, including an improved determination of efficiency, and to reduce the reactor induced background systematics.

VII. SENSITIVITY TO THE PLUTONIUM CONTENT OF THE CORE

With the end of the Cold War, hundreds of tons of weapon-grade plutonium were determined to be surplus to U.S. and Russian defence needs. In April 2010 the US and Russian governments signed a protocol amending the 2000 Plutonium Management and Disposition Agreement (PMDA), which commits each country to dispose of no less than 34 metric tons (MT) of excess weapon-grade plutonium and envisions disposition of more weapon-grade plutonium over time. The combined amount, 68 MT, represents enough material for several thousands of nuclear weapons. The current approach is to transform the weapon-grade plutonium into mixed oxide fuel and irradiate it in reactors. We study here how a small neutrino detector like Nucifer could monitor this kind of operation to guarantee that plutonium is really being burnt in the reactor.

The neutrino rate measured by Nucifer is used as a calibration point for a nuclear fuel highly enriched in ^{235}U with 92 % of the fissions coming from this isotope (see section III). This approach can be seen as a measurement of our absolute normalization with the statistical 2.5 % accuracy (from $281 \pm 7(stat) \pm 18(syst)\,\overline{\nu}_e$/day) provided by our sample.

Using the MCNP Utility for Reactor Evolution

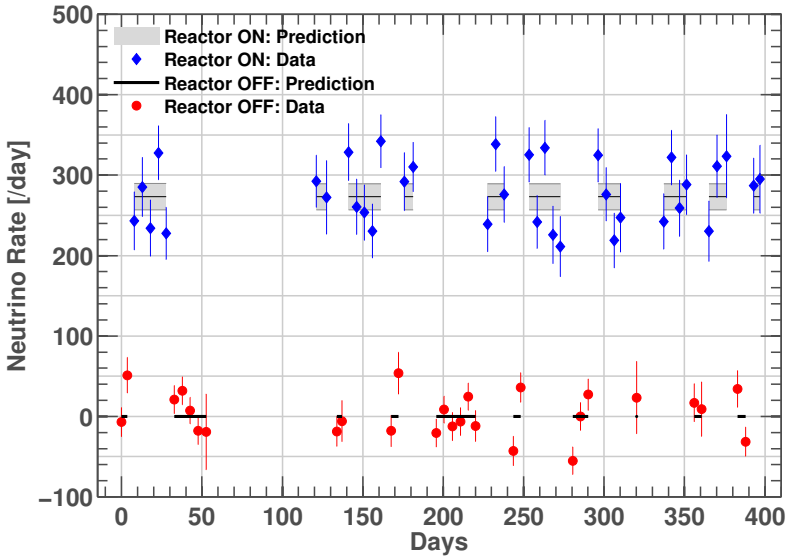

FIG. 13. Antineutrino rate measurement monitoring the Osiris nuclear reactor operations. Each data point (blue diamonds) corresponds to about 5 days of data taking with its associated statistical uncertainty. The grey shaded area is the rate expectation above the mean correlated background when the reactor is OFF, referred as zero level here and plotted as red dots.

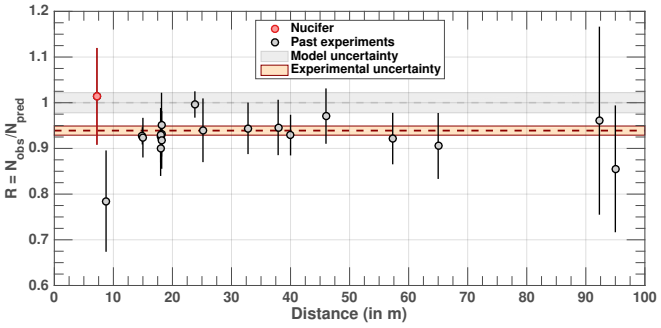

FIG. 14. Comparison of the Nucifer measurement of $R_\nu^{\rm obs}/R_\nu^{\rm pred}$ with others short baseline experiments and the average value of the RAA [5]. Without Nucifer, the average ratio is 0.938 ± 0.024 ($2.6\,\sigma$), and with Nucifer the average is 0.940 ± 0.024 ($2.5\,\sigma$).

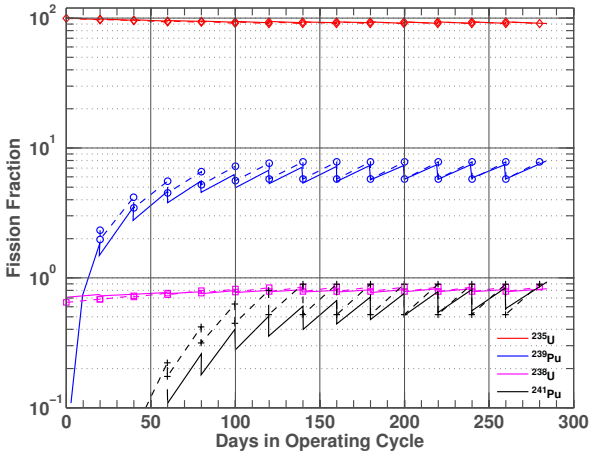

FIG. 15. Fission fraction in % of each fissile isotopes, ^{235}U, ^{238}U, ^{239}Pu, and ^{241}Pu, as predicted by the MURE simulation (solid lines) [31]. Here the core is initially filled with fresh fuel and its isotopic composition evolves for 14 cycles, but all actual Osiris cycles correspond to the equilibrium regime. The dotted lines illustrate the effective approach dedicated to study the sensitivity to the ^{239}Pu mass in the core after it is tuned to reproduce the reference MURE results.

(MURE) [32, 33], we were able to simulate the evolution of the Osiris fuel with a full 3D Monte-Carlo simulation. Figure 15 shows an example of the evolution of the fission fractions of ^{235}U, ^{238}U, ^{239}Pu, and ^{241}Pu as predicted by MURE [31]. Starting from a fresh uranium fuel enriched at 19.75 % an equilibrium is reached after the 7^{th} cycle. As expected the fission of the ^{235}U dominates by far and all fission fraction evolutions during a cycle are moderate.

We then simulated the operation of the Osiris reactor with part of its fuel elements loaded with ^{239}Pu, like in UOX-MOX fuel. The MURE simulation of the fuel evolution being very time consuming, we used for this purpose a simple model of the core [34]: we solved the Bateman's equations of the evolution of the uranium and plutonium isotopes assuming a uniform neutron flux adjusted to match the mean Osiris thermal power and with effective nuclear cross sections (n-capture and fission) cal-

ibrated to reproduce the MURE simulation results. Figure 15 shows that a good agreement could be reached for the nominal core composition of Osiris, good enough for the purpose of this study.

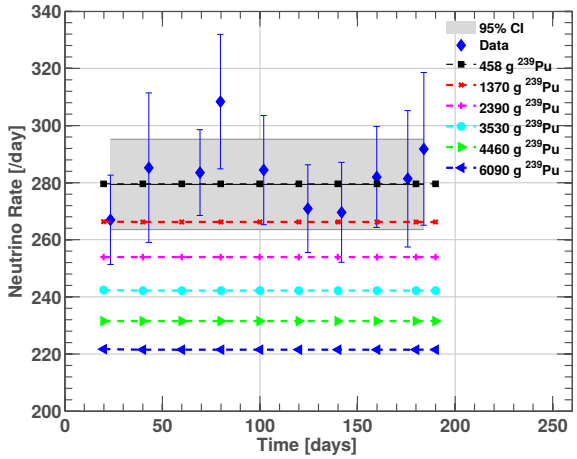

FIG. 16. Mean neutrino rate detected by Nucifer (blue diamonds), concatenating Osiris cycles. The grey area shows the interval at 95 % C.L. The other horizontal lines illustrate the predicted evolution of the detected flux for an increasing mass of Plutonium in the Osiris core.

In standard operation the Osiris core is loaded with 14.00 ± 0.75 kg of ^{235}U and 450 ± 50 g of ^{239}Pu, the error bar representing the variation of the masses around these mean values during a 21 days cycle. This equilibrium is reached after an initial load of about 20 kg of ^{235}U. To study the impact of plutonium content on the detected neutrino flux we tried various initial configurations with up to 10 kg of Pu in the initial composition of the core. However the initial mass of all fissile materials (mainly ^{235}U and ^{239}Pu) was always kept equal to 20 kg for all configurations. Then we simulated the reactor core evolution during several cycles at constant full power, until the equilibrium was reached. At this stage we determined the associated mean mass of ^{239}Pu in the core from the number of atoms predicted by our model. Finally, the mean neutrino rate was computed from the number of fissions per isotope in our model and from the reference ratios of detected $\overline{\nu}_e$ per ^{235}U fission listed in table VI.

Isotope	^{235}U	^{238}U	^{239}Pu	^{241}Pu
Relative $\overline{\nu}_e$ rate	1	1.512	0.635	0.900

TABLE VI. Variation of detected antineutrino rate per fission normalized to one fission of ^{235}U. The reference antineutrino spectra per fission are taken from [3] and [4] and interaction cross-section from [19]. The prompt energy cuts of the Nucifer analysis are applied corresponding to $2.78\,\text{MeV} < E_{\overline{\nu}_e} < 7.88\,\text{MeV}$.

As expected the neutrino rate decreases as the mass of ^{239}Pu in the core, hence the contribution of ^{239}Pu fissions, increases. This is illustrated in figure 16 where a global normalization factor is applied to our model in order to set the prediction for the nominal core composition equal to the observed rate. Then assuming the same data taking period and background conditions, the detection of a lower $\overline{\nu}_e$ rate with 95 % confidence level is equivalent to a drop of 2.23 times of our current rate uncertainty (7.1), i.e. 15.8 less detected $\overline{\nu}_e$ per day. This sensitivity limit is reached for about 1.5 kg of ^{239}Pu in the core, a mass representing 10 % of the total mass of fissioning elements in the Osiris core at equilibrium. As already stated before, this sensitivity is driven by the large accidental background at the Osiris site. If the same Nucifer detector was installed close to a commercial reactor with a baseline (25 m) and background conditions (S/B=4) similar to the SONGS experiment [35], the same sensitivity could be reached in less than 3 days.

VIII. CONCLUSION AND OUTLOOK

This article reported on the features and performances of the Nucifer experiment operating at the Saclay research centre of the French Alternative Energies and Atomic Energy Commission (CEA) since Spring 2012. The experimental configuration, the Osiris research nuclear reactor, and the detector setup have been presented.

We discussed the installation and the operation of the detector 7.21 ± 0.11 m away from the Osiris reactor, making Nucifer the second world-shortest baseline neutrino experiment ever being operated. Being at such shot distance of the core lead to great difficulty in mitigating and controlling reactor induced accidental background. The high-accuracy measurement and subtraction of the huge gamma-ray reactor induced background was validated, as well as a novel method for assessing cosmic ray induced backgrounds at very shallow depth, correcting for the evolution of the atmospheric pressure during reactor OFF/ON periods.

Eventually reactor antineutrinos at very short baselines can be used to probe the Reactor Antineutrino Anomaly and to search for possible oscillations into sterile neutrino species. However, because of the current lack of precision in the emitted neutrino flux as well as the large accidental background level, no definitive conclusion could be obtained yet. A more refined evaluation of the expected neutrino rate would be necessary through further improvements of the detector response modelling, which are beyond the scope of this paper. Nevertheless Nucifer data can be now included into global analyses and it could perhaps constrain some of the still-allowed oscillation scenarios at short baselines. Dedicated experiments are clearly necessary to confirm or reject the short baseline oscillation hypothesis, such as the Stereo [36], Neutrino-4 [37], PROSPECT [38], or SOX [39, 40] experiments expected in the next months or years.

The detection efficiency was improved by a factor of 3 with respect to past reactor neutrino experiments dedicated to nuclear safeguards, reaching a mean daily rates of about 300 $\overline{\nu}_e$/day with a cubic-meter scale target volume. Therefore, the achieved statistics is large enough to be of interest for cooperative monitoring regimes. Nucifer has also shown a great stability, suitable for relative monitoring of the neutrino rate within a few percent, and safe automatic operation for a few years with only little occasional maintenance. Hence, this operation regime approaches the requirements of any IAEA monitoring apparatus, making a Nucifer-like antineutrino detector suitable to monitor and safeguard nuclear reactors.

As a first societal application, and within the framework of the Plutonium Management and Disposition Agreement for the disposal of Weapon-grade plutonium, we illustrated the possibility of monitoring the plutonium content in the Osiris core by showing that Nucifer could detect the presence of about 1.5 kg of Pu at 95 % C.L, based on the actual data. This result would be improved with Nucifer deployed further away from a more powerful core, by intrinsically lowering the dominant gamma-ray accidental background component.

ACKNOWLEDGEMENTS

We are indebted to the management and staff of CEA/DEN/Osiris reactor for their full support towards the realization of the Nucifer experiment and the excellent support they provided to the Nucifer collaboration during the detector operation; we acknowledge the support the CEA/DSM, CEA/DAM, CEA/DEN, CNRS/IN2P3, and the Max Planck Gesellschaft. We would like to thank Gabriele Fioni for initiating the collaboration between CEA physicists and the OSIRIS reactor staff.

[1] Burn-up or fuel utilization is the amount of energy extracted from a given quantity of nuclear fuel.
[2] Th. A. Mueller *et al.*, Phys. Rev. **C83**, 054615 (2011), arXiv:hep-ex/1101.2663 [hep-ex].
[3] P. Huber, Phys.Rev. **C84**, 024617 (2011), arXiv:hep-ph/1106.0687 [hep-ph].
[4] N. Haag, A. Gtlein, M. Hofmann, L. Oberauer, W. Potzel, *et al.*, Phys.Rev.Lett. **112**, 122501 (2014), arXiv:nucl-ex/1312.5601 [nucl-ex].
[5] G. Mention *et al.*, Phys. Rev. **D83**, 073006 (2011), arXiv:1101.2755 [hep-ex].
[6] T. Lasserre, Phys. Dark Univ. **4**, 81 (2014), arXiv:hep-ex/1404.7352 [hep-ex].
[7] F. A. Nezrick and F. Reines, Phys. Rev. **142**, 852 (1966).
[8] D. Silverman and A. Soni, Phys. Rev. **D27**, 58 (1983).
[9] H. Kwon *et al.*, Phys. Rev. **D24**, 1097 (1981).
[10] A. Hummada, S. Lazrak Mikou, M. Avenier, G. Bagieu, J. Cavaignac, and D. Koang, Applied Radiation and Isotopes **46**, 449 (1995).
[11] U.S. Department of State, "2000 plutonium management and disposition agreement," (2010), fact Sheet, `http://www.state.gov/r/pa/prs/ps/2010/04/140097.htm`.
[12] Direction de l'énergie nucléaire, Direction déléguée aux affaires nucléaires de Saclay, Département des réacteurs et services nucléaires, "The Osiris reactor," Les Éditions stratégiques (2005), `http://www-cadarache.cea.fr/rjh/Add-On/osiris_gb.pdf`.
[13] J.-F. Parisot, ed., *Research Nuclear Reactors*, CEA Saclay and Éditions du Moniteur ed. (2012) `http://www.materials.cea.fr/en/PDF/Research%20nuclear%20reactors_CEA-en.pdf`.
[14] Brookhaven National Laboratory, "National nuclear data center," Information extracted from the Chart of Nuclides database, `http://www.nndc.bnl.gov/`.
[15] C. Aberle *et al.*, JINST **7**, P06008 (2012), arXiv:1112.5941 [physics.ins-det].
[16] V. Kopeikin, L. Mikaelyan, and V. Sinev, Phys. Atom. Nucl. **67**, 1892 (2004), arXiv:hep-ph/0410100 [hep-ph].
[17] J. Pelzer, *Démarrage de l'expérience Nucifer, un détecteur d'antineutrinos miniature placé à 7m du cœur du réacteur Osiris*, Master's thesis, École Polytechnique (2012), CEA Saclay - Irfu / 201200003730, `http://www-ist.cea.fr/publicea/exl-doc/201200003730.pdf`.
[18] Nuclear Energy Agency, "TRIPOLI-4.3.3 and 4.4, Coupled Neutron, Photon, Electron, Positron 3-D, Time Dependent Monte-Carlo, Transport Calculation," (2009), `http://www.oecd-nea.org/tools/abstract/detail/NEA-1716/`.
[19] A. Strumia and F. Vissani, Phys. Lett. **B564**, 42 (2003), arXiv:astro-ph/0302055 [astro-ph].
[20] K. Schreckenbach, G. Colvin, W. Gelletly, and F. Von Feilitzsch, Phys.Lett. **B160**, 325 (1985).
[21] A. A. Hahn, K. Schreckenbach, G. Colvin, B. Krusche, W. Gelletly, *et al.*, Phys.Lett. **B218**, 365 (1989).
[22] T. A. Nghiem, *Data Analysis for the Nucifer Antineutrino Detection Experiment*, Master's thesis, University of Cambridge (2013), CEA Saclay - Irfu / 201500003287, `http://www-ist.cea.fr/publicea/exl-doc/201500003287.pdf`.
[23] Y. Abe *et al.* (Double Chooz), Phys.Rev. **D87**, 011102 (2013), arXiv:hep-ex/1210.3748 [hep-ex].
[24] F. Clark, *An Exponential Transform as an Importance Sampling Device: A Review*, ORNL (Series) No. ORNL-RSIC-14 (Oak Ridge National Laboratory, P.O. Box 2008, Oak Ridge, TN 37831, 1966).
[25] G. O'Rielly, N. Kolb, and R. Pywell, Nuclear Instruments and Methods in Physics Research Section A: Accelerators, Spectrometers, Detectors and Associated Equipment **368**, 745749 (1996).
[26] B. von Krosigk *et al.*, Eur. Phys. J. **C73**, 2390 (2013), arXiv:1301.6403 [astro-ph.IM].
[27] N. Soppera, M. Bossant, and E. Dupont, Nuclear Data Sheets **120**, 294 (2014).
[28] R. Koch and H. H. Thies, Nucl. Phys. **A272**, 296 (1976).

[29] M. Berger *et al.*, "XCOM: Photon Cross Sections Database," National Institute of Standards and Technology, http://www.nist.gov/pml/data/xcom/index.cfm.

[30] A. Collin, *Étude des antineutrinos de réacteurs : mesure de l'angle de mélange leptonique et recherche d'éventuels neutrinos stériles*, Ph.D. thesis, Université Paris Sud - Paris XI (2014).

[31] V. M. Bui, *La décroissance bêta des produits de fission pour la non-prolifération et la puissance résiduelle des réacteurs*, Ph.D. thesis, École des Mines de Nantes (2013), https://tel.archives-ouvertes.fr/tel-00834225.

[32] O. Meplan *et al.*, in *European Nuclear Conference 2005* (2005) Nuclear Power for the XXIst Century: From basic research to high-tech industry.

[33] Nuclear Energy Agency, "MURE, MCNP Utility for Reactor Evolution: couples Monte-Carlo transport with fuel burnup calculations," (2009), http://www.oecd-nea.org/tools/abstract/detail/nea-1845.

[34] X. Joubert, *Étude des caractéristiques d'un liquide scintillant dopé au gadolinium et développement d'un code d'interpolation FIASCO*, Master's thesis, ENSICAEN (2009), CEA Saclay - Irfu / 201200003743, http://www-ist.cea.fr/publicea/exl-doc/201200003743.pdf.

[35] N. S. Bowden *et al.*, Nucl. Instrum. Meth. **A572**, 985 (2007).

[36] V. Helaine, (2016), nuPhys2015 (London, 16-18 December 2015), arXiv:1604.08877 [physics.ins-det].

[37] A. P. Serebrov *et al.*, J. Exp. Theor. Phys. **121**, 578 (2015), [Zh. Eksp. Teor. Fiz.148,no.4,665674(2015)].

[38] J. Ashenfelter *et al.* (PROSPECT), (2015), arXiv:1512.02202 [physics].

[39] G. Bellini *et al.* (Borexino), JHEP **1308**, 038 (2013), arXiv:1304.7721 [physics].

[40] I. Machulin (Borexino), Proceedings of the 16th Lomonosov Conference on Elementary Particle Physics: Particle Physics at the Year of Centenary of Bruno Pontecorvo , 48 (2015).